Research Square

Preprints are preliminary reports that have not undergone peer review.
They should not be considered conclusive, used to inform clinical practice,
or referenced by the media as validated information.

Coherent light emission and electrical tuning of WS2-WSe2 interlayer excitons

Lukas Novotny

lnovotny@ethz.ch

ETH Zurich https://orcid.org/0000-0002-9970-8345

Shengyu Shan

ETH Zurich https://orcid.org/0000-0001-5865-3694

Antti Moilanen

University of Eastern Finland https://orcid.org/0000-0002-9888-8524

Jonas Ziegler

ETH Zurich https://orcid.org/0000-0002-2683-5124

Qia Lin

ETH Zurich

Guodong Xue

Peking University

Karolina Łempicka-Mirek

Photonics Laboratory, ETH Zurich https://orcid.org/0000-0003-0838-2990

David Callegari

PSI

Takashi Taniguchi

Research Center for Materials Nanoarchitectonics, National Institute for Materials Science
https://orcid.org/0000-0002-1467-3105

Kenji Watanabe

National Institute for Materials Science https://orcid.org/0000-0003-3701-8119

Kirsten Moselund

Paul Scherrer Institut, EPFL

Kaihui Liu

State Key Laboratory for Mesoscopic Physics, Frontiers Science Center for Nano-optoelectronics, School of Physics, Peking University https://orcid.org/0000-0002-8781-2495

Simone Iadanza

PSI

Article

Keywords: transition metal dichalcogenides, van der Waals materials, coherent light sources, photonic crystal cavities

Posted Date: June 16th, 2026

DOI: https://doi.org/10.21203/rs.3.rs-9912305/v1

License: This work is licensed under a Creative Commons Attribution 4.0 International License.
Read Full License

Additional Declarations: There is **NO** Competing Interest.

Coherent light emission and electrical tuning of WS_2-WSe_2 interlayer excitons

Shengyu Shan[1†], Antti J. Moilanen[1,2*†], Jonas D. Ziegler[1], Qia Lin[1], Guodong Xue[3], Karolina Łempicka-Mirek[1], David R. Callegari[4], Takashi Taniguchi[5], Kenji Watanabe[6], Kirsten Moselund[4], Kaihui Liu[3], Simone Iadanza[4], Lukas Novotny[1*]

[1*]Photonics Laboratory, ETH Zürich, 8093, Zürich, Switzerland.
[2*]Center for Photonics Sciences, University of Eastern Finland, 80100, Joensuu, Finland.
[3]State Key Laboratory for Mesoscopic Physics, Frontiers Science Center for Nano-optoelectronics, School of Physics, Peking University, Beijing, 100871, China.
[4]Paul Scherrer Institute, 5232 Villigen, Switzerland.
[5]Research Center for Materials Nanoarchitectonics, National Institute for Materials Science, 1-1 Namiki, Tsukuba 305-0044, Japan.
[6]Research Center for Electronic and Optical Materials, National Institute for Materials Science, 1-1 Namiki, Tsukuba 305-0044, Japan.

*Corresponding author(s). E-mail(s): antti.moilanen@uef.fi; lnovotny@ethz.ch;
†These authors contributed equally to this work.

Abstract

Coherent on-chip light sources are essential components for integrated photonics, enabling interference-based logic, high-fidelity signal routing, and precision sensing. Two-dimensional (2D) materials offer a promising platform for realizing ultracompact light sources because they combine strong excitonic effects, broad material compatibility, and efficient electrical tunability. However, achieving simultaneous optical performance and stable electrical controllability is hindered by cavity geometry and electrode-induced optical losses. Here, we introduce a hybrid hexagonal boron nitride (hBN)–silicon nitride (Si_3N_4) photonic crystal cavity coupled to a WS_2–WSe_2 heterobilayer. The system features high-Q optical modes and provides robust electrical integration. We demonstrate coherent

light emission from cavity-coupled WS_2–WSe_2 interlayer excitons, with coherence lengths exceeding 5 mm, the size of a typical photonic integrated circuit. Furthermore, by integrating MoS_2 as low-loss electrodes, we show that the exciton emission can be spectrally tuned and brought in resonance with the cavity mode, without deteriorating its quality factor ($\boldsymbol{Q > 1200}$). The combination of our hybrid cavity design with low-loss electrodes is a promising platform for on-chip light sources and 2D optoelectronics.

Keywords: transition metal dichalcogenides, van der Waals materials, coherent light sources, photonic crystal cavities

Introduction

The rapid development of information technology demands fast and efficient data processing, positioning photonic integrated circuits as a central platform for next-generation on-chip information systems. A crucial challenge in photonic integration is the realization of compact, energy-efficient, and coherent on-chip light sources. Moreover, next-generation photonic systems require active tunability to enable dynamic wavelength and power control, spectral multiplexing, and reconfigurable photonic circuits. Realizing efficient coherent light emission on a silicon platform, however, is hindered by silicon's indirect bandgap and the lattice-mismatch constraints encountered when integrating conventional III–V semiconductors [1–3]. In addition, bulk semiconductors suffer from strong dielectric screening that suppresses efficient electrical modulation. Two-dimensional (2D) semiconductors—most notably the transition-metal dichalcogenides (TMDs)—offer a promising route to overcome these limitations. Their atomically thin nature and van der Waals (vdW) bonding enable integration on arbitrary substrates without lattice-matching constraints, while the absence of dielectric screening allows highly efficient electrical tunability of their excitonic resonances [4]. Together, these properties open new opportunities for compact and tunable on-chip coherent light sources [5–7].

Early demonstrations employed monolayer TMDs as the gain medium for coherent light emission [7–14]. More recently, coherent light emission has been reported using interlayer excitons in heterobilayer TMDs including $WSe_2/MoSe_2$ [15, 16] and WSe_2/MoS_2 [17, 18], but the combination WS_2/WSe_2 has so far not been investigated. Interlayer excitons in type-II band-aligned heterostructures possess emission energies below the bandgaps of the individual layers, resulting in negligible optical absorption [19] and enabling the system to maintain a high cavity quality factor (Q factor). Among the possible combinations, WS_2/WSe_2 stands out as an attractive platform for studying interlayer excitons and realizing exciton-based light sources [20]. The relatively large geometric lattice mismatch between the layers (∼4% [21]) suppresses mesoscopic atomic reconstruction [22], leading to spatially uniform and spectrally homogeneous interlayer exciton emission [23, 24]. Furthermore, interlayer excitons possess an out-of-plane dipole moment, enabling direct electrical tuning of their emission wavelength via the quantum-confined Stark effect [25, 26].

Despite these advantages, achieving electrical tunability within a high-Q cavity remains challenging due to fundamental trade-offs between optical performance and electrical integration. While various cavity architectures have been explored for TMD-based light sources [14, 27], only a few implementations have successfully integrated electrical control [26–30]. Significant limitations remain due to two primary challenges. First, many high-Q resonators such as disk and ring cavities rely on mechanically isolated geometries; integrating them with planar electrodes inherently compromises spatial mode overlap and structural stability. Second, standard metallic or semimetallic electrodes inevitably introduce optical absorption that degrades the cavity Q factor.

Results

Device architecture

Figure 1**a** presents a schematic of the device with a cross-section in the x–z plane. From top to bottom, a vdW heterostructure consisting of top hBN (∼80 nm)/WS_2/WSe_2/bottom hBN (∼20 nm) is placed on a ∼200 nm thick Si_3N_4 layer deposited on a silicon substrate. Subsequently, the holes of the photonic crystal cavity are patterned through the entire vdW–Si_3N_4 stack, with a total thickness of approximately 300 nm. Finally, the vdW-Si_3N_4 cavity is suspended by under-etching the silicon substrate via the holes (Methods and Supplementary Note 1).

Both Si_3N_4 and hBN possess refractive indices near 2 in the 800–900 nm wavelength range, allowing them to be treated as optically equivalent media in the photonic crystal cavity design [16, 31]. The Si_3N_4/Si substrate enables straightforward integration and cavity suspension, while the hBN layers preserve the flexibility of vdW heterostructure assembly and provide a pristine dielectric environment for the gain medium. Compared to previously reported hBN–Si_3N_4 hybrid cavities based on one-dimensional (1D) nanobeam geometries [16, 31], our 2D photonic crystal cavity provides improved mechanical robustness.

The cavity design prioritizes a high Q factor and optimal spatial overlap with the gain medium. To maximize confinement in the low-refractive-index Si_3N_4 system, we employed a dispersion-adapted 2D photonic crystal cavity design [32]. A scanning electron microscope image of a fabricated cavity on the hBN–Si_3N_4 stack is shown in Fig. 1**b**, with a lattice constant $a = 340$ nm and a hole radius $r = 85$ nm in the design. Additional details on the cavity optimization and resonance tuning are provided in Supplementary Note 2. The defect line at the cavity center features a smoothly tapered width to suppress out-of-plane radiation loss. Figure 1**c** presents the simulated electric field distribution in the x–y plane of a cavity mode with a Q factor of $\sim 10^7$. The corresponding electric field intensity profile along the z direction at the cavity center is shown in Fig. 1**d**. With top and bottom hBN thicknesses of ∼80 nm and ∼20 nm, respectively, the gain medium is located close to the cavity center (approximately 70 nm from the mid-plane), corresponding to about 70% of the field maximum. This configuration ensures good spatial overlap between the optical mode and the gain medium.

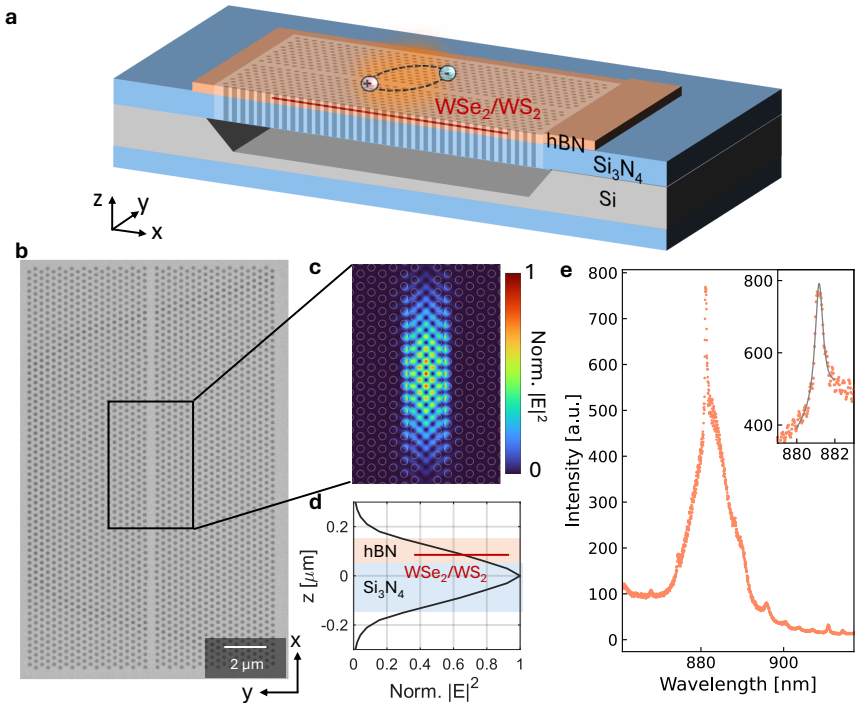


Fig. 1 **a**, Schematic of a hBN–Si_3N_4 2D photonic crystal cavity with integrated WSe_2–WS_2 heterobilayer. The cavity is patterned by electron beam lithography, etched through the hBN–TMD-Si_3N_4 stack, and suspended by under-etching the Si substrate. **b**, Scanning electron microscope image of a reference hBN–Si_3N_4 cavity with a designed lattice constant $a = 340$ nm and hole radius $r = 85$ nm. **c**, Simulated electric field distribution of the cavity fundamental TE mode in the x–y plane. **d**, Corresponding electric field intensity profile along the z direction at the cavity center. **e**, Cavity-coupled WSe_2–WS_2 interlayer exciton spectrum with a sharp resonance near 881 nm (sample A). Cavity parameters are identical as the sample shown in **b**. Inset: zoom-in of the resonance, fitted with a Lorentzian function and a linear background, linewidth about 0.5 nm. Cryogenic PL was measured at ∼5 K using a 633 nm continuous-wave (CW) laser (53 µW) focused at the cavity center (Methods).

Figure 1**e** presents a representative photoluminescence (PL) spectrum from the WS_2/WSe_2 heterobilayer inside the cavity. The broad emission originates from interlayer excitons, while the sharp peak near 881 nm corresponds to the exciton emission coupled to the cavity resonance. A Lorentzian fit of the cavity resonance reveals a linewidth of approximately 0.5 nm (Fig. 1**e**, inset). To enhance the signal-to-noise ratio for free-space detection, the emitted signal is collected from a scattering site fabricated near the cavity edge (Methods and Supplementary Note 3).

Pre-characterization of interlayer exciton

Besides spatial overlap, precise spectral alignment is essential to efficiently couple interlayer exciton emission to the cavity mode. However, the interlayer exciton energy in WS_2/WSe_2 heterobilayers varies with twist angle and excitation power [24, 33,

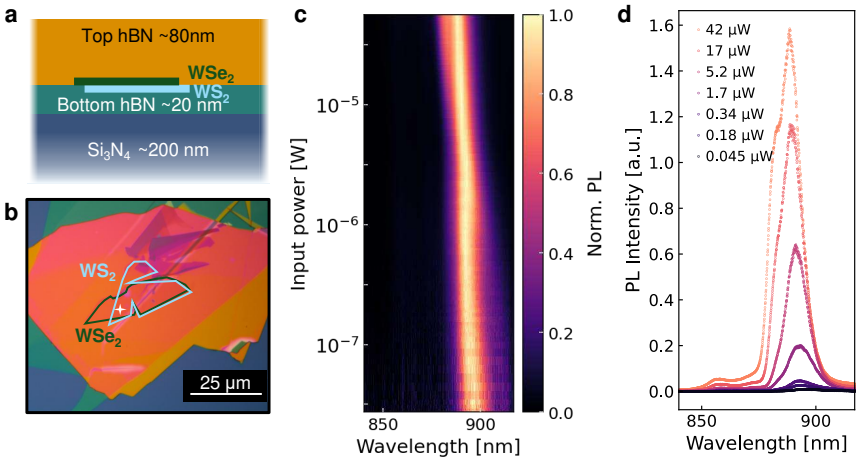


Fig. 2 **a**, Schematic of the vdW stack on a Si_3N_4 substrate. **b**, Optical microscope image of the vdW stack (sample A) containing WSe_2–WS_2 heterobilayer on Si_3N_4. The outlines of WS_2 and WSe_2 are indicated by light blue and dark green lines, respectively. The excitation laser is focused at the position marked by a star. **c**, Power-dependent photoluminescence (PL) spectra of the interlayer exciton measured at the position shown in **b** and normalized to their respective maxima. The excitation source is a CW laser at 633 nm. **d**, PL spectra at representative excitation powers.

34, 34, 35], introducing additional complexity for spectral alignment. Our fabrication flow overcomes this limitation by enabling the characterization of interlayer exciton emission prior to cavity patterning.

Figures 2**a** and **b** show the schematic and optical image of a vdW stack (sample A) before cavity fabrication. For the active area, we use exfoliated WS_2 and WSe_2 monolayers and align the sharp edges to ensure angle-aligned heterostructure to maximize PL emission. Power-dependent PL spectra from the region marked in Fig. 2**b** are presented in Figs. 2**c** and **d**. At an excitation power of ∼45 nW, the PL peak is centered near 895 nm, and it blue-shifts to around 887 nm at ∼42 µW. We attribute this shift to dipolar exciton–exciton repulsion, which directly depends on the average distance between excitons [34, 36]. Consequently, the cavity resonance is designed to align with the blue-shifted emission at higher excitation powers to ensure coupling at high exciton densities.

Cavity integration and emerging coherence

Figure 3**a** shows the optical microscope image of sample A after patterning the cavity geometry into the vdW stack. To assess the lasing behavior, we first characterized the cavity-coupled interlayer excitons using power-dependent PL measurements. The PL spectra were recorded under various excitation powers, and the amplitude and linewidth of the cavity resonance near 881 nm were extracted for each spectrum. The light-in–light-out (L–L) curve is shown in Fig. 3**b**. The output exhibits a slope greater than 1 on a log-log scale over the 1.6 µW–12 µW range. This superlinear increase indicates a nonlinear gain response of cavity-coupled interlayer excitons. To better quantify

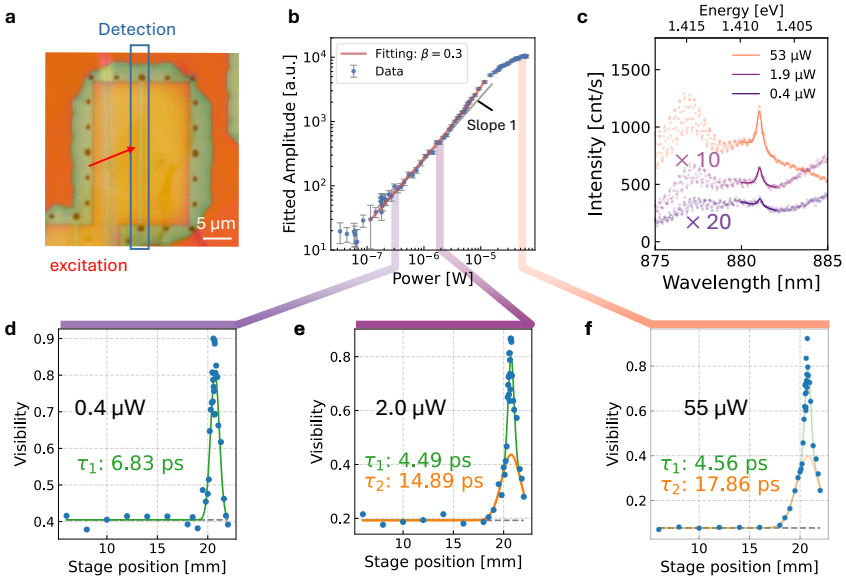


Fig. 3 Power-dependent output intensity and temporal coherence measurements. **a**, Optical image of sample A after cavity fabrication. The cavity center is aligned with the position marked by a star in Fig. 2**b**. A 633 nm CW laser excites the cavity center (red arrow), with emission collected along the defect line. **b**, Cavity-mode amplitude as a function of excitation power. The red curve shows a rate-equation fit yielding $\beta = 0.3$. **c**, Representative PL spectra (dots) with corresponding Lorentzian fits (solid lines). **d**–**f**, Coherence measurements of the cavity resonance at indicated excitation powers. In **d**, the fringe visibility is fitted with a single Gaussian plus a constant background, $y = a_0 + a_1 e^{-(x-b)^2/\sigma_1^2}$ (green curve), where a_0 is the background (grey dashed line) and σ_1 relates to coherence time τ_1. In **e** and **f**, the data are fitted with two Gaussian components: $y = a_0 + a_1 e^{-(x-b)^2/\sigma_1^2} + a_2 e^{-(x-b)^2/\sigma_2^2}$. The grey dashed line represents the constant background a_0, the orange curve shows the sum of the second Gaussian and the background ($a_0 + a_2 e^{-(x-b)^2/\sigma_2^2}$), and the green curve represents the total fit. The extracted coherence times $\tau_{1,2}$ (calculated from $\sigma_{1,2}$) are indicated in each panel, following Eq. S1 in the Supplementary Note 5.

this nonlinear behavior, we fitted the L–L curve using a standard laser rate-equation model, yielding spontaneous emission coupling efficiency (β factor) of approximately 0.3. This high β arises from placing the atomically thin gain medium in the cavity's high-field region, enabling efficient coupling. Details regarding the model and fitting parameters are provided in the Supplementary Note 4. Representative PL spectra recorded at excitation powers below, within, and above the nonlinear regime are presented in Fig. 3**c**. We note that various factors, such as exciton saturation, exciton-exciton annihilation, and power-dependent exciton energy shifts, affect the emission slope. Nonlinear increases in power dependence can originate from stimulated emission, which is associated with the emergence of long-range temporal coherence (the onset of lasing). To directly measure the coherence time, we implemented a Michelson interferometer. To isolate the cavity mode from the broad emission background, the interferometer output was coupled into a spectrometer. This spectral filtering enhances the signal-to-noise ratio (SNR) and enables the determination of the cavity-mode

coherence time, provided the linewidth is narrower than the spectrometer's resolution ($\sim 0.38\,\mathrm{nm}$).

The measured fringe visibility relates directly to the temporal autocorrelation function of the incident field. For an incident electric field, the autocorrelation function, also called the *coherence function*, is $\langle E^*(t)E(t+\tau)\rangle_t$, where $\langle\cdot\rangle_t$ indicates the time average with respect to t. τ is the time delay and $E(t)$ is the positive frequency part of the electric field. The *power spectral density* $S(\omega)$ of the field is the Fourier transform of the autocorrelation function:

$$S(\omega) = \frac{1}{2\pi}\int_{-\infty}^{\infty} \langle E^*(t)E(t+\tau)\rangle_t e^{i\omega\tau}\, d\tau \tag{1}$$

We model the emission as a narrow Gaussian peak centered at ω_0, superimposed on a broad background S_B:

$$S(\omega) = S_B + S_0 e^{-\frac{(\omega-\omega_0)^2}{\sigma_\omega^2}}, \tag{2}$$

In this expression, S_0 is the spectral amplitude of the coherent emission and $2\sqrt{\ln 2}\sigma_\omega$ represents the full width at half maximum (FWHM) linewidth. For a spectrometer resolution (defined by the single-pixel bandwidth) of $\Delta\omega$, and in the limit of $2\sqrt{\ln 2}\sigma_\omega \ll \Delta\omega$, the fringe visibility $\hat{V}(\Delta t, \omega)$ can be expressed as:

$$\begin{aligned}\hat{V}(\Delta t,\omega) \propto\; & S_B\,\Delta\omega\,\varepsilon_0 c\,\mathrm{sinc}\left(\frac{\Delta\omega\Delta t}{2}\right) \\ & + \sqrt{\pi}\,\varepsilon_0 c\frac{\sigma_\omega S_0}{2} e^{-\sigma_\omega^2\Delta t^2/4}\end{aligned} \tag{3}$$

Here, Δt is the time delay between the two optical paths of the interferometer, ε_0 is the vacuum permittivity, and c is the speed of light in vacuum. In this framework, the filtered broad background produces a rapid visibility decay governed by the spectrometer resolution limit. Conversely, the narrow coherent feature manifests as a second, slowly decaying component. While the analytical derivation for an ideal rectangular filter yields a sinc function, the actual experimental filtering profile is tapered. We therefore fit the visibility data using two Gaussian components to extract the intrinsic cavity coherence. Supplementary Note 5 details the derivations and measurement protocol, while Supplementary Note 9 provides numerical validation and measurements of a reference sample.

We measured the coherence time at three excitation powers: $0.4\,\mu\mathrm{W}$ (below the threshold of nonlinear intensity increase), $2.0\,\mu\mathrm{W}$ (within the nonlinear increase regime), and $55\,\mu\mathrm{W}$ (above the threshold). Below threshold, as shown in Fig. 3d, the fringe visibility can be fitted with single Gaussian function, yielding a coherence time of $6.95\,\mathrm{ps}$. Using the relation between linewidth and coherence time (τ_{coh}),

$$\tau_{\mathrm{coh}} \cdot \Delta\lambda_{\mathrm{FWHM}} = 8\ln 2\,\frac{\lambda_0^2}{2\pi c}, \tag{4}$$

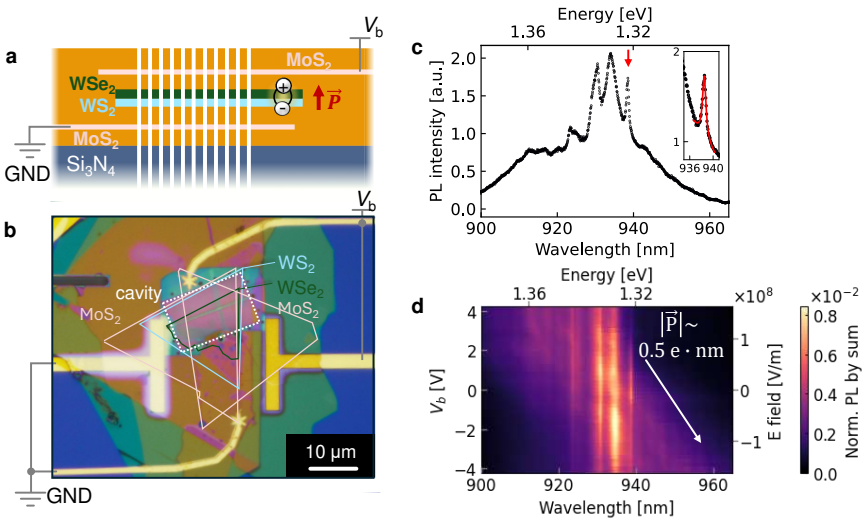


Fig. 4 **a**, Cross-section and **b**, optical microscope image of the device (sample B). The stack comprises, from top to bottom: hBN (40 nm), MoS_2, hBN (23 nm), WSe_2, WS_2, hBN (23 nm), MoS_2, and hBN (12 nm). Four TMD flakes are labeled and their outlines are drawn with corresponding colors. **c**, PL spectrum of cavity coupled interlayer exciton without applied voltage. Inset: zoom-in of the resonance, fitted with a Lorentzian function and a linear background, linewidth about 0.74 nm. **d**, PL spectra of cavity coupled interlayer exciton under different bias voltages. Each spectrum was normalized to the sum of all photons in the row. Spectra in **c** and **d** both were measured under 633 nm CW laser excitation, ~ 20 nW pumping power.

we derive a linewidth of 0.33 nm. When the excitation power is increased to 2 µW (Fig. 3**e**), a second Gaussian component emerges, corresponding to a longer coherence time of 14.89 ps and a linewidth of 0.15 nm. The shorter component, with a coherence time of 4.49 ps, originates from the spectrometer-filtered background. At even higher excitation power of 55 µW, the coherence time further increases to 17.86 ps, resulting in a coherence length over 5 mm. It corresponds to a linewidth of 0.13 nm—more than a twofold reduction compared to the initial linewidth. This significant coherence increase is consistent with the Schawlow–Townes relation [37], suggesting the onset of lasing.

As detailed in Supplementary Note 8, we estimate the exciton density to be $\sim 4 \times 10^{10}\,\mathrm{cm}^{-2}$ (generation rate $\sim 4 \times 10^{19}\,\mathrm{cm}^{-2}\,\mathrm{s}^{-1}$) at an excitation power of ~ 7.2 µW. Comparing the output light emission intensity to the input pump power, we infer that our results are consistent with the system reaching the lasing threshold [14]; however, the calculation (see Supplementary Note 6) involves uncertainties, especially concerning the out-coupling efficiency from the scatterer and the quantum yield of the TMDs.

Electrical tuning

So far, the hBN-Si_3N_4 hybrid photonic crystal cavity has been used as a passive system for TMD integration. A key advantage of our architecture, however, is the stable integration of electrodes. Here, we introduce electrode integration within the

cavity, which enables active post-fabrication tuning of the spectral alignment between the exciton emission and the cavity modes. Crucially, we employ monolayer MoS_2 as electrodes to minimize the optical losses.

Monolayer MoS_2 has a bandgap much larger than the interlayer exciton emission energy and therefore introduces only minimal absorption loss to the cavity resonance. In contrast, using a monolayer graphene electrode strongly quenches the cavity resonance and reduces the Q factor (see Supplementary Note 10 for details). As illustrated in Fig. 4**a**, sample B incorporates two monolayer MoS_2 flakes as electrodes to generate a vertical electric field across the WSe_2/WS_2 heterobilayer, enabling electrical tuning of the interlayer exciton energy via the quantum-confined Stark effect.

Figure 4**b** displays the optical microscope image of sample B. Each MoS_2 electrode is contacted using an edge contact (star-shape, Cr/Au) and a bottom contact (T-shape, Cr/Au) to ensure electrical connection. The photonic crystal cavity is patterned throughout the entire stack, with the cavity center positioned in the overlap region of all four TMD flakes. In this device, all four TMD flakes are grown by chemical vapor deposition (CVD), which provides larger flake areas and facilitates good rotational alignment during the stacking process. Prior to cavity patterning, the interlayer exciton emission from the heterobilayer is measured to lie in the wavelength range of 900–950 nm, which is more red-shifted compared to Sample A. This shift is likely due to differences of band alignment in the CVD-grown WSe_2 and WS_2 compared to the exfoliated ones. Accordingly, the cavity design is adjusted to produce a correspondingly red-shifted resonance.

A representative PL spectrum of cavity-coupled interlayer exciton is shown in Fig. 4**c**. The cavity mode near 938 nm exhibits a linewidth of $\sim$0.74 nm, corresponding to a quality factor of $Q > 1200$. This Q factor is slightly lower than that of the device shown in Fig. 1. We attribute this reduction largely to interfacial bubbles in the stack caused by polymer residue during the transfer of the CVD-grown TMDs, alongside the small but finite optical losses introduced by the integrated MoS_2 electrodes. Consequently, we anticipate that achieving cleaner vdW interfaces will further improve the Q factor in future devices. By applying a bias across the two MoS_2 electrodes, we are able to tune the interlayer exciton energy via the Stark effect (Fig. 4**d**). The cavity resonances remain unchanged under bias, while the electric field shifts the exciton transition energies.

Under a positive bias voltage V_b, the vertical electric field $\mathbf{E}$ is antiparallel to the out-of-plane dipole moment $\mathbf{P}$ of the interlayer exciton. The dipole experiences additional potential energy $\Delta U = -\mathbf{P} \cdot \mathbf{E}$. This potential energy increases the exciton energy for $V_\mathrm{b} > 0$ (blueshift) and decreases it for negative bias (redshift). The electric field inside the TMD layers is given by [25]

$$|\mathbf{E}| = \frac{V_\mathrm{b}}{t_\mathrm{total}} \frac{\varepsilon_\mathrm{hBN}}{\varepsilon_\mathrm{TMD}}, \tag{5}$$

where $\varepsilon_\mathrm{hBN} = 3.9$ and $\varepsilon_\mathrm{TMD} = 7.2$ are the permittivities for hBN and TMD layers. The tuning trace indicated by the white arrow corresponds to an estimated out-of-plane dipole moment of $|\mathbf{P}| = 0.5\,\mathrm{e} \cdot \mathrm{nm}$, in close agreement with the expected value, which is $0.6\,\mathrm{e} \cdot \mathrm{nm}$ [38].

Apart from the wavelength tuning, the interlayer exciton PL intensity decreases with increasing applied bias for both positive and negative polarities and exhibits irregular discontinuities. These changes likely originate from carrier injection and subsequent modifications to moiré unit cell filling factors [39]. Additionally, increased carrier density may enhance non-radiative recombination [34], further reducing the PL intensity at higher bias. Detailed analysis and PL spectra without normalization are provided in Supplementary Note 7.

Conclusions

In summary, we have developed an hBN–Si_3N_4 hybrid 2D photonic crystal cavity tailored for TMD integration and demonstrated the emergence of coherent light emission from WSe_2–WS_2 interlayer excitons. The connected cavity geometry provides enhanced mechanical stability, enabling robust electrode integration and active control. The cavity-coupled interlayer exciton PL exhibits a nonlinear increase in output intensity with pump power, accompanied by an increase in coherence length to over 5 mm—more than twice the limit set by the cavity Q factor in the low-power regime. Following the criteria outlined for state-of-the-art TMD-based micro- and nanolasers [14] and the laser checklist proposed by *Nature Photonics* [40], our system fulfills two of the three key indicators for lasing: (i) threshold behavior and (ii) highly coherent emission. Although linewidth narrowing above threshold cannot be conclusively demonstrated due to measurement limitations, the temporal coherence measurements support the interpretation of emerging stimulated emission. We can rule out common alternative explanations for the observed emission characteristics. Cavity-filtered spontaneous emission cannot account for the observed nonlinear input–output response or the pump-induced increase in coherence length. Amplified spontaneous emission (ASE) would typically lead to spectral broadening with increasing pump power and coherence lengths far shorter than the 5 mm observed here, and no ASE-like spectral evolution is detected. These considerations support the interpretation that the observed behavior reflects the onset of stimulated emission rather than artifacts of cavity filtering or ASE. Among other common lasing characteristics, directional emission and polarized emission remain unresolved due to the use of a scatterer for out-coupling the emission. A definitive measurement of second-order correlations will be essential in future work to fully establish the laser characteristics of TMD-based systems.

Building on the mechanical stability of this cavity architecture, we further advance beyond passive light-emitting systems to demonstrate active electrical control. We achieve post-fabrication electrical tuning of the spectral alignment between the interlayer excitons and the cavity resonances while maintaining a high Q factor. To mitigate the optical losses typically introduced by metallic or semimetallic electrodes, we introduce MoS_2 as low-loss electrodes. The integration of CVD-grown TMDs further highlights the potential for scalable device fabrication. In future work, electrical excitation methods [41–43] could be combined with low-loss TMD electrodes to realize electrically driven coherent light sources. Integrating these components is essential for the transition toward practical on-chip optoelectronic technologies. Together, these

results establish a new platform for 2D-material-based coherent light sources and electrically tunable on-chip optoelectronic circuits.

Methods

Substrate preparation

Double-side polished silicon wafers (200 µm) coated with low-pressure CVD Si_3N_4 (∼200 nm) on both sides purchased from MicroChemicals GmbH were used as substrates (Article number: WNA40200105B1314S202). Metal markers and electrodes (Cr/Au, 10 nm/100 nm) were deposited using electron-beam lithography with a poly(methyl methacrylate) (PMMA) resist. Chromium was selected for its strong adhesion and excellent etching resistance to the chemicals used in subsequent steps, including concentrated base solutions. The substrates were cleaned to remove organic residues using warm acetone and a subsequent O_2 plasma treatment. Selected substrates were immersed in a 1:50 diluted hydrofluoric acid (HF) solution for 30 s, followed by a 90 s rinse in deionized water and nitrogen drying. This HF treatment enhances the adhesion between the hBN and the Si_3N_4 substrate during the potassium hydroxide (KOH) underetching process. For substrates not treated with HF, thermal annealing was used to improve adhesion. All processed substrates were stored in an argon environment to prevent oxidation.

2D heterostructure assembly

Multilayer hBN flakes and monolayer TMDs were mechanically exfoliated onto SiO_2/Si substrates unless otherwise noted. Monolayer TMDs were identified by optical contrast, while hBN flake thicknesses were determined using atomic force microscopy (AFM). For sample B, CVD monolayer TMDs were grown on sapphire substrates based on methods described in [44, 45] and transferred to a secondary SiO_2/Si carrier substrate for the stacking process. This transfer utilized a PMMA supporting layer, and the TMDs were delaminated from the growth substrate using water assistance. After transfer, the PMMA was removed in acetone. Following this procedure, the TMDs became compatible with the standard dry-transfer technique and could be picked up reproducibly at temperatures between 70 °C and 85 °C.

The vdW stacks were assembled by a curved polydimethylsiloxane (PDMS) stamp covered with a polycarbonate (PC) film inside an argon-filled glovebox [46]. The top hBN was picked up as the first layer to encapsulate the whole device. Different crystal flakes were picked up sequentially according to the design, and then the stack was transferred to a Si_3N_4 substrate. Finally, the PC film was dissolved in chloroform.

MoS_2 Contact

For devices requiring MoS_2 electrodes (Sample B), bottom Cr/Au contacts were prepatterned on the substrate. Additional edge contacts to the MoS_2 were fabricated after the heterostructure stacking based on methods described in [47]. Chromium was utilized instead of titanium for the adhesion layer to ensure compatibility with the final KOH underetching process.

Photonic crystal cavity fabrication

Photonic crystal cavities were defined using electron-beam lithography. The patterned structures were transferred through the vdW stack and the underlying silicon nitride layer using a combination of inductively coupled plasma reactive ion etching and standard reactive ion etching. Following the removal of the resist, the devices were suspended by immersing them in a KOH aqueous solution to selectively underetch the substrate. A comprehensive fabrication protocol detailing the lithography procedures and etching parameters is provided in Supplementary Note 1.

Optical and optoelectronic characterization
Photoluminescence (PL) measurements of the $WS_2 - WSe_2$ interlayer excitons were performed at cryogenic temperatures (4–6 K) using a closed-cycle cryostat (Attocube AttoDry 800). The sample was mounted face up on a cooling stage. The photoluminescence was excited and collected from above using an air objective with a numerical aperture of 0.81 located inside the cooling chamber. The collected signal passed through an optical window, and a 700 nm long-pass filter was employed to suppress the excitation laser. Spectra were recorded using a spectrometer (Andor SR303) equipped with a charge-coupled device camera (Andor iDus 416). Unless otherwise specified, a 633 nm continuous-wave (CW) laser was used for excitation. For time-resolved measurements and specific Supplementary experiments, a pulsed laser diode (Picoquant LDH-D-C-640) with central wavelength of 640 nm was utilized. To characterize the cavity resonance, a grating of 1200 l/mm, 850 nm blaze was selected in the spectrometer. The entrance slit width was set to 100 µm for the power-dependence measurements of the cavity mode and 150 µm for the Michelson interferometry measurements. Interlayer exciton lifetimes were determined via time-resolved photoluminescence utilizing an avalanche photodiode coupled with a time-correlated single-photon counting module (PicoHarp 300). For electrically tunable PL measurements, the bias was applied and monitored using a picoammeter/voltage source (Keithley 6482).

Characterization of the bare silicon nitride cavity resonances was performed using a secondary setup at room temperature. This approach facilitated rapid design verification and lithographic tuning (Supplementary Note 2). The sample was mounted on a customized inverted microscope (Nikon TE300) equipped with a piezoelectric stage. A 100x air objective (Nikon, NA 0.9) was utilized to focus the excitation laser onto the sample and collect the resulting optical signal. All room temperature spectra were recorded using a Princeton Instruments Acton SpectraPro 300i spectrometer.

Cavity resonance fitting
Cavity resonances are fitted using a Lorentzian function and a linear background $y = A\frac{\gamma^2/4}{(\lambda-\lambda_0)^2+\lambda^2/4} + k\lambda + b$, where A is the amplitude, γ is the full-width at half maximum (FWHM), λ is the wavelength, λ_0 is the resonance wavelength, and k and b describe the linear background.

Acknowledgments

This work has been supported by the Swiss National Science Foundation (grant 200020_192362/1) and the ETH Grant SYNEMA ETH-15 19-1. A.J.M., J.D.Z, and K.Ł.-M. acknowledge financial support by the ETH Zürich Postdoctoral Fellowship

programme. G.X. acknowledges support from the National Natural Science Foundation of China (grant T24B2001). K.W. and T.T. acknowledge support from the CREST (JPMJCR24A5), JST and World Premier International Research Center Initiative (WPI), MEXT, Japan. The authors are grateful for the help from Maurice Friedrichs, Yang Xu, Jiwoo Oh, Nicola Carlon Zambon, Petra Burkard, and Armin Knoll in developing the fabrication process and device configuration. We thank Annarita Di Toma, and Salim Turki for the help in cavity design and simulation. We thank Dănuț-Valentin Dinu and Fabien Dorey for the help in building the optical measurement setup and automating the measurements. We thank Mingchao Ding, Achint Jain, and Martin Frimmer for fruitful discussions and support. The use of the facilities of the FIRST center for micro- and nanoscience at ETH Zürich and Binnig and Rohrer Nanotechnology Center are gratefully acknowledged.

Supplementary information

Supplementary Notes 1–10, Figs. S1–S14 and text references.

References

[1] Ma, R.-M., Oulton, R.F. Applications of nanolasers. Nature Nanotechnology **14**, 12–22 (2019) https://doi.org/10.1038/s41565-018-0320-y

[2] Jeong, K.-Y., Hwang, M.-S., Kim, J., Park, J.-S., Lee, J.M., Park, H.-G. Recent Progress in Nanolaser Technology. Advanced Materials **32**(51), 2001996 (2020) https://doi.org/10.1002/adma.202001996

[3] Han, Y., Park, H., Bowers, J., Lau, K.M. Recent advances in light sources on silicon. Advances in Optics and Photonics **14**(3), 404–454 (2022) https://doi.org/10.1364/AOP.455976

[4] Mueller, T., Malic, E. Exciton physics and device application of two-dimensional transition metal dichalcogenide semiconductors. npj 2D Materials and Applications **2**, 29 (2018) https://doi.org/10.1038/s41699-018-0074-2

[5] Wang, G., Chernikov, A., Glazov, M.M., Heinz, T.F., Marie, X., Amand, T., Urbaszek, B. Colloquium: Excitons in atomically thin transition metal dichalcogenides. Reviews of Modern Physics **90**(2), 021001 (2018) https://doi.org/10.1103/RevModPhys.90.021001

[6] Liu, D.-S., Wu, J., Xu, H., Wang, Z. Emerging Light-Emitting Materials for Photonic Integration. Advanced Materials **33**(4), 2003733 (2021) https://doi.org/10.1002/adma.202003733

[7] Wen, W., Wu, L., Yu, T. Excitonic Lasers in Atomically Thin 2D Semiconductors. ACS Materials Letters **2**(10), 1328–1342 (2020) https://doi.org/10.1021/acsmaterialslett.0c00277

[8] Ye, Y., Wong, Z.J., Lu, X., Ni, X., Zhu, H., Chen, X., Wang, Y., Zhang, X. Monolayer excitonic laser. Nature Photonics **9**(11), 733–737 (2015) https://doi.org/10.1038/nphoton.2015.197

[9] Wu, S., Buckley, S., Schaibley, J.R., Feng, L., Yan, J., Mandrus, D.G., Hatami, F., Yao, W., Vučković, J., Majumdar, A., Xu, X. Monolayer semiconductor nanocavity lasers with ultralow thresholds. Nature **520**(7545), 69–72 (2015) https://doi.org/10.1038/nature14290

[10] Li, Y., Zhang, J., Huang, D., Sun, H., Fan, F., Feng, J., Wang, Z., Ning, C.Z. Room-temperature continuous-wave lasing from monolayer molybdenum ditelluride integrated with a silicon nanobeam cavity. Nature Nanotechnology **12**(10), 987–992 (2017) https://doi.org/10.1038/nnano.2017.128

[11] Shang, J., Cong, C., Wang, Z., Peimyoo, N., Wu, L., Zou, C., Chen, Y., Chin, X.Y., Wang, J., Soci, C., Huang, W., Yu, T. Room-temperature 2D semiconductor activated vertical-cavity surface-emitting lasers. Nature Communications **8**, 543 (2017) https://doi.org/10.1038/s41467-017-00743-w

[12] Zhao, L., Shang, Q., Gao, Y., Shi, J., Liu, Z., Chen, J., Mi, Y., Yang, P., Zhang, Z., Du, W., Hong, M., Liang, Y., Xie, J., Hu, X., Peng, B., Leng, J., Liu, X., Zhao, Y., Zhang, Y., Zhang, Q. High-Temperature Continuous-Wave Pumped Lasing from Large-Area Monolayer Semiconductors Grown by Chemical Vapor Deposition. ACS Nano **12**(9), 9390–9396 (2018) https://doi.org/10.1021/acsnano.8b04511

[13] Ge, X., Minkov, M., Fan, S., Li, X., Zhou, W. Laterally confined photonic crystal surface emitting laser incorporating monolayer tungsten disulfide. npj 2D Materials and Applications **3**, 16 (2019) https://doi.org/10.1038/s41699-019-0099-1

[14] López-Carrasco, T., Guimarães, M.H.D. Atomically thin transition metal dichalcogenide nanolasers: Challenges and opportunities. Applied Physics Letters **126**(22), 220501 (2025) https://doi.org/10.1063/5.0267478

[15] Paik, E.Y., Zhang, L., Burg, G.W., Gogna, R., Tutuc, E., Deng, H. Interlayer exciton laser of extended spatial coherence in atomically thin heterostructures. Nature **576**(7785), 80–84 (2019) https://doi.org/10.1038/s41586-019-1779-x

[16] Qian, C., Troue, M., Figueiredo, J., Soubelet, P., Villafañe, V., Beierlein, J., Klembt, S., Stier, A.V., Höfling, S., Holleitner, A.W., Finley, J.J. Lasing of moiré trapped MoSe2/WSe2 interlayer excitons coupled to a nanocavity. Science Advances **10**(2), 6359 (2024) https://doi.org/10.1126/sciadv.adk6359

[17] Liu, Y., Fang, H., Rasmita, A., Zhou, Y., Li, J., Yu, T., Xiong, Q., Zheludev, N., Liu, J., Gao, W. Room temperature nanocavity laser with interlayer excitons in 2D heterostructures. Science Advances **5**(4), 4506 (2019) https://doi.org/10.1126/sciadv.aav4506

[18] Lin, Q., Fang, H., Kalaboukhov, A., Liu, Y., Zhang, Y., Fischer, M., Li, J., Hagel, J., Brem, S., Malic, E., Stenger, N., Sun, Z., Wubs, M., Xiao, S. Moiré-engineered light-matter interactions in MoS2/WSe2 heterobilayers at room temperature. Nature Communications **15**, 8762 (2024) https://doi.org/10.1038/s41467-024-53083-x

[19] Wu, F., Lovorn, T., MacDonald, A.H. Theory of optical absorption by interlayer excitons in transition metal dichalcogenide heterobilayers. Physical Review B **97**(3), 035306 (2018) https://doi.org/10.1103/PhysRevB.97.035306

[20] Fu, Q., Liu, X., Wang, S., Wu, Z., Xia, W., Zhang, Q., Ni, Z., Hu, Z., Lu, J. Room-temperature efficient and tunable interlayer exciton emissions in WS_2 /WSe_2 heterobilayers at high generation rates. Optics Letters **49**(18), 5196 (2024) https://doi.org/10.1364/OL.534473

[21] Schutte, W.J., De Boer, J.L., Jellinek, F. Crystal structures of tungsten disulfide and diselenide. Journal of Solid State Chemistry **70**(2), 207–209 (1987) https://doi.org/10.1016/0022-4596(87)90057-0

[22] Zhao, S., Li, Z., Huang, X., Rupp, A., Göser, J., Vovk, I.A., Kruchinin, S.Y., Watanabe, K., Taniguchi, T., Bilgin, I., Baimuratov, A.S., Högele, A. Excitons in mesoscopically reconstructed moiré heterostructures. Nature Nanotechnology **18**(6), 572–579 (2023) https://doi.org/10.1038/s41565-023-01356-9

[23] Jin, C., Regan, E.C., Yan, A., Iqbal Bakti Utama, M., Wang, D., Zhao, S., Qin, Y., Yang, S., Zheng, Z., Shi, S., Watanabe, K., Taniguchi, T., Tongay, S., Zettl, A., Wang, F. Observation of moiré excitons in WSe2/WS2 heterostructure superlattices. Nature **567**(7746), 76–80 (2019) https://doi.org/10.1038/s41586-019-0976-y

[24] Yuan, L., Zheng, B., Kunstmann, J., Brumme, T., Kuc, A.B., Ma, C., Deng, S., Blach, D., Pan, A., Huang, L. Twist-angle-dependent interlayer exciton diffusion in WS2–WSe2 heterobilayers. Nature Materials **19**(6), 617–623 (2020) https://doi.org/10.1038/s41563-020-0670-3

[25] Jauregui, L.A., Joe, A.Y., Pistunova, K., Wild, D.S., High, A.A., Zhou, Y., Scuri, G., De Greve, K., Sushko, A., Yu, C.-H., Taniguchi, T., Watanabe, K., Needleman, D.J., Lukin, M.D., Park, H., Kim, P. Electrical control of interlayer exciton dynamics in atomically thin heterostructures. Science **366**(6467), 870–875 (2019) https://doi.org/10.1126/science.aaw4194

[26] Lopriore, E., Tagarelli, F., Fitzgerald, J.M., Gonzalez Marin, J.F., Watanabe, K., Taniguchi, T., Malic, E., Kis, A. Enhancing interlayer exciton dynamics by coupling with monolithic cavities via the field-induced Stark effect. Nature Nanotechnology **20**(10), 1412–1418 (2025) https://doi.org/10.1038/s41565-025-01969-2

[27] Ren, T., Águila, A., Chen, Z., Xu, Q., Zhou, X., Duan, R., Grzeszczyk, M.,

Gong, X., Watanabe, K., Taniguchi, T., Novoselov, K.S., Koperski, M., Sun, H. Van der Waals photonic integrated circuit with coherent light generation. Nature Communications **16**, 5931 (2025) https://doi.org/10.1038/s41467-025-60778-2

[28] Liu, C.-H., Clark, G., Fryett, T., Wu, S., Zheng, J., Hatami, F., Xu, X., Majumdar, A. Nanocavity Integrated van der Waals Heterostructure Light-Emitting Tunneling Diode. Nano Letters **17**, 200–205 (2017) https://doi.org/10.1021/acs.nanolett.6b03801

[29] Chen, Z.-Z., Lin, H.-T., Chang, C.-Y., Adil, M., Tsai, P.-C., Kao, T.S., Chen, C., Lin, S.-Y., Shih, M.-H. Electrically-Driven 2D Semiconductor Microcavity Laser. Advanced Materials **37**(42), 09861 (2025) https://doi.org/10.1002/adma.202509861

[30] Moilanen, A.J., Cavigelli, M., Taniguchi, T., Watanabe, K., Novotny, L. Electrical Control of Photoluminescence in 2D Semiconductors Coupled to Plasmonic Lattices. ACS Nano **19**(4), 4731–4738 (2025) https://doi.org/10.1021/acsnano.4c15459

[31] Fröch, J.E., Kim, S., Mendelson, N., Kianinia, M., Toth, M., Aharonovich, I. Coupling Hexagonal Boron Nitride Quantum Emitters to Photonic Crystal Cavities. ACS Nano **14**(6), 7085–7091 (2020) https://doi.org/10.1021/acsnano.0c01818

[32] Welna, K., Portalupi, S.L., Galli, M., O'Faolain, L., Krauss, T.F. Novel Dispersion-Adapted Photonic Crystal Cavity With Improved Disorder Stability. IEEE Journal of Quantum Electronics **48**(9), 1177–1183 (2012) https://doi.org/10.1109/JQE.2012.2204960

[33] Wu, K., Zhong, H., Guo, Q., Tang, J., Zhang, J., Qian, L., Shi, Z., Zhang, C., Yuan, S., Zhang, S., Xu, H. Identification of twist-angle-dependent excitons in WS2/WSe2 heterobilayers. National Science Review **9**(6), 135 (2022) https://doi.org/10.1093/nsr/nwab135

[34] Chatterjee, S., Dandu, M., Dasika, P., Biswas, R., Das, S., Watanabe, K., Taniguchi, T., Raghunathan, V., Majumdar, K. Harmonic to anharmonic tuning of moiré potential leading to unconventional Stark effect and giant dipolar repulsion in WS2/WSe2 heterobilayer. Nature Communications **14**, 4679 (2023) https://doi.org/10.1038/s41467-023-40329-3

[35] Cai, C.-S., Lai, W.-Y., Liu, P.-H., Chou, T.-C., Liu, R.-Y., Lin, C.-M., Gwo, S., Hsu, W.-T. Ultralow Auger-Assisted Interlayer Exciton Annihilation in WS2/WSe2 Moiré Heterobilayers. Nano Letters **24**(9), 2773–2781 (2024) https://doi.org/10.1021/acs.nanolett.3c04688

[36] Montblanch, A.R.-P., Kara, D.M., Paradisanos, I., Purser, C.M., Feuer, M.S.G., Alexeev, E.M., Stefan, L., Qin, Y., Blei, M., Wang, G., Cadore, A.R., Latawiec, P., Lončar, M., Tongay, S., Ferrari, A.C., Atatüre, M. Confinement of long-lived

interlayer excitons in WS2/WSe2 heterostructures. Communications Physics **4**, 119 (2021) https://doi.org/10.1038/s42005-021-00625-0

[37] Schawlow, A.L., Townes, C.H. Infrared and Optical Masers. Physical Review **112**(6), 1940–1949 (1958) https://doi.org/10.1103/PhysRev.112.1940

[38] Yu, L., Pistunova, K., Hu, J., Watanabe, K., Taniguchi, T., Heinz, T.F. Observation of quadrupolar and dipolar excitons in a semiconductor heterotrilayer. Nature Materials **22**(12), 1485–1491 (2023) https://doi.org/10.1038/s41563-023-01678-y

[39] Lian, Z., Meng, Y., Ma, L., Maity, I., Yan, L., Wu, Q., Huang, X., Chen, D., Chen, X., Chen, X., Blei, M., Taniguchi, T., Watanabe, K., Tongay, S., Lischner, J., Cui, Y.-T., Shi, S.-F. Valley-polarized excitonic Mott insulator in WS2/WSe2 moiré superlattice. Nature Physics **20**, 34–39 (2024) https://doi.org/10.1038/s41567-023-02266-2

[40] Scrutinizing lasers. Nature Photonics **11**(3), 139–139 (2017) https://doi.org/10.1038/nphoton.2017.28

[41] Khelifa*, R., Shan*, S., Moilanen, A.J., Taniguchi, T., Watanabe, K., Novotny, L. WSe2 Light-Emitting Device Coupled to an h-BN Waveguide. ACS Photonics **10**(5), 1328–1333 (2023) https://doi.org/10.1021/acsphotonics.2c01963

[42] Dorey*, F., Ziegler*, J.D., Moilanen, A.J., Hordiichuk, O., Nagamine, G., Taniguchi, T., Watanabe, K., Norris, D.J., Kovalenko, M.V., Rainò, G., Novotny, L. Transferable Plasmonic Arrays Enabling Strong Coupling with Layered Perovskites in an Active Diode Architecture. Nano Letters (2025) https://doi.org/10.1021/acs.nanolett.5c04569 . Publisher: American Chemical Society

[43] Ziegler, J.D., Papadopoulos, S., Moilanen, A.J., Martínez, M., Lin, Q., Mosina, K., Taniguchi, T., Watanabe, K., Sofer, Z., Dirnberger, F., Novotny, L. Electrical excitation of self-hybridized exciton polaritons in a van der Waals antiferromagnet. Science Advances **11**(45), 6724 (2025) https://doi.org/10.1126/sciadv.adz6724

[44] Zuo, Y., Liu, C., Ding, L., Qiao, R., Tian, J., Liu, C., Wang, Q., Xue, G., You, Y., Guo, Q., Wang, J., Fu, Y., Liu, K., Zhou, X., Hong, H., Wu, M., Lu, X., Yang, R., Zhang, G., Yu, D., Wang, E., Bai, X., Ding, F., Liu, K. Robust growth of two-dimensional metal dichalcogenides and their alloys by active chalcogen monomer supply. Nature Communications **13**, 1007 (2022) https://doi.org/10.1038/s41467-022-28628-7

[45] Xue, G., Sui, X., Yin, P., Zhou, Z., Li, X., Cheng, Y., Guo, Q., Zhang, S., Wen, Y., Zuo, Y., Zhao, C., Wu, M., Gao, P., Li, Q., He, J., Wang, E., Zhang, G., Liu, C., Liu, K. Modularized batch production of 12-inch transition metal dichalcogenides by local element supply. Science Bulletin **68**(14), 1514–1521 (2023) https://doi.org/10.1016/j.scib.2023.06.037

[46] Zomer, P.J., Guimarães, M.H.D., Brant, J.C., Tombros, N., Van Wees, B.J. Fast pick up technique for high quality heterostructures of bilayer graphene and hexagonal boron nitride. Appl. Phys. Lett. **105**, 013101 (2014)

[47] Jain, A., Szabó, Á., Parzefall, M., Bonvin, E., Taniguchi, T., Watanabe, K., Bharadwaj, P., Luisier, M., Novotny, L. One-Dimensional Edge Contacts to a Monolayer Semiconductor. Nano Letters **19**(10), 6914–6923 (2019) https://doi.org/10.1021/acs.nanolett.9b02166

Supplementary Files

This is a list of supplementary files associated with this preprint. Click to download.

- SupplementaryInfoCoherentlightemissionandelectricaltuningofWS2WSe2interlayerexcitons.pdf